Research on Telescope TTL Coupling Noise in Intersatellite Laser Interferometry

Zhi WANG[1†*], Tao YU[1†], Ya ZHAO[1,2], Ziren LUO[3], Wei SHA[1], Chao FANG[1],
Yukun WANG[1], Shaoxin WANG[1], Keqi QI[1], Yongxian WANG[1], and Xuanwen XU[4]

[1]*Changchun Institute of Optics, Fine Mechanics and Physics, Chinese Academy of Sciences, Changchun 130033, China*

[2]*University of Chinese Academy of Sciences, Beijing 100049, China*

[3]*Institute of Mechanics, Chinese Academy of Sciences, Beijing 100190, China*

[4]*Jilin University, Changchun 130022, China*

†*These authors contributed equally to this work*

*Corresponding author: Zhi WANG   E-mail: wz070611@126.com

Abstract: The detection mission of gravitational waves in space is that the accuracy of the long-baseline intersatellite laser interferometry on the million-kilometer order needs to reach the order of $8\,\mathrm{pm}/\sqrt{\mathrm{Hz}}$. Among all noise sources that affect the interferometry accuracy, tilt-to-length (TTL) coupling noise is the second largest source of noise after shot noise. This paper focuses on studying the contribution of TTL coupling noise of the telescope system in the intersatellite scientific interferometer. By referring to the laser interferometer space antenna (LISA)'s noise budget, TTL coupling noise is required to be within $\pm 25\,\mu\mathrm{m/rad}$ ($\pm 300\,\mu\mathrm{rad}$). Therefore, this paper focuses on studying both the mechanism of TTL coupling noise due to the noise sources of the telescope and the method of suppressing the TTL noise, which can lay a foundation for noise distribution and the development of engineering prototypes in subsequent tasks.

Keywords: Intersatellite laser interferometry; telescope; TTL coupling noise

1. Introduction

In the "Taiji Program in Space" of the Chinese Academy of Sciences, three satellites in the formation of an equilateral triangle constitute a space-based gravitational wave observatory, which runs in the orbit around the Sun. The center of mass of three satellites falls on the Earth's orbit and the satellite spacing is 3 million kilometers. Each satellite contains two test masses. For free floating motion of the test masses, the satellites will use the drag-free control technology to protect the test masses against non-conservative force disturbance. A laser link is adopted between the satellites to measure the relative motion between different satellite test masses by laser interferometry. When gravitational waves pass, the distance between the test masses will change. This distance change will be read by the laser interferometry system to invert the gravitational wave signal [1, 2].

The change in the distance between the satellites on the million-kilometer arm length is realized

through heterodyne interferometry by using a pair of telescopes at the top of the interfering arm [3]. According to the gravitational wave strain formula $h = \Delta L / L$, the million-kilometer arm length is used to improve the sensitivity of gravitational strain. Even with such a long baseline, the accuracy of measuring the distance change is still extremely demanding. The total displacement noise budget of the interferometry system is in the order of $8\,\mathrm{pm}/\sqrt{\mathrm{Hz}}$, covering any noise source that may affect the measurement. The second largest source of noise stems from the coupling noise between the angular jitter of the interfering beams and the optical path readout, called tilt-to-length (TTL) coupling.

For the study of TTL coupling noise, the Albert Einstein Institute (AEI) in Germany has done a lot of work [4, 5]. However, the telescope in the AEI experimental system only simulated a tilted beam that could rotate, which was far from enough [6, 7]. After the telescope was in the orbit, changes in structural parameters (launch process overload, temperature gradient, stress release under microgravity, material outgassing, etc.) led to distortions in the exit pupil wavefronts, therefore bringing in extra TTL coupling noise even with imaging system. This paper will analyze the mechanism of generating TTL noise due to the telescope system for the first time in the world.

2. TTL coupling noise

2.1 Research on the introduction of TTL by the telescope system

2.1.1 Analysis of far-field wavefronts

After being expanded by the local telescope, the fundamental-mode Gaussian beam emitted by the local laser propagates for 3×10^9 kilometer is received by the remote telescope. The beam propagation satisfies the Fraunhofer diffraction:

$$E(x, y, z) = -\frac{\mathrm{j}}{\lambda z} \mathrm{e}^{\mathrm{j}k\left(\frac{x^2+y^2}{2z}+z\right)} \iint_{\Sigma} E(x',y',0) \mathrm{e}^{\mathrm{j}k\frac{xx'+yy'}{z}} \mathrm{d}x'\mathrm{d}y'$$

$$(1)$$

where $E(x,y,\mathrm{z})$ is the diffracted far light filed after a long distance, $E(x',y',0)$ is the light field at the exit pupil of the transmitting telescope, which is the fundamental-mode Gaussian beam, k is wave number, and λ is wavelength. It is known that circular aperture Fraunhofer diffraction of the fundamental-mode Gaussian beam is similar to the plane wave. To simplify calculation, the light field distribution at the exit pupil is regarded as an ideal plane wave, namely $E(x', y', 0) = 1$.
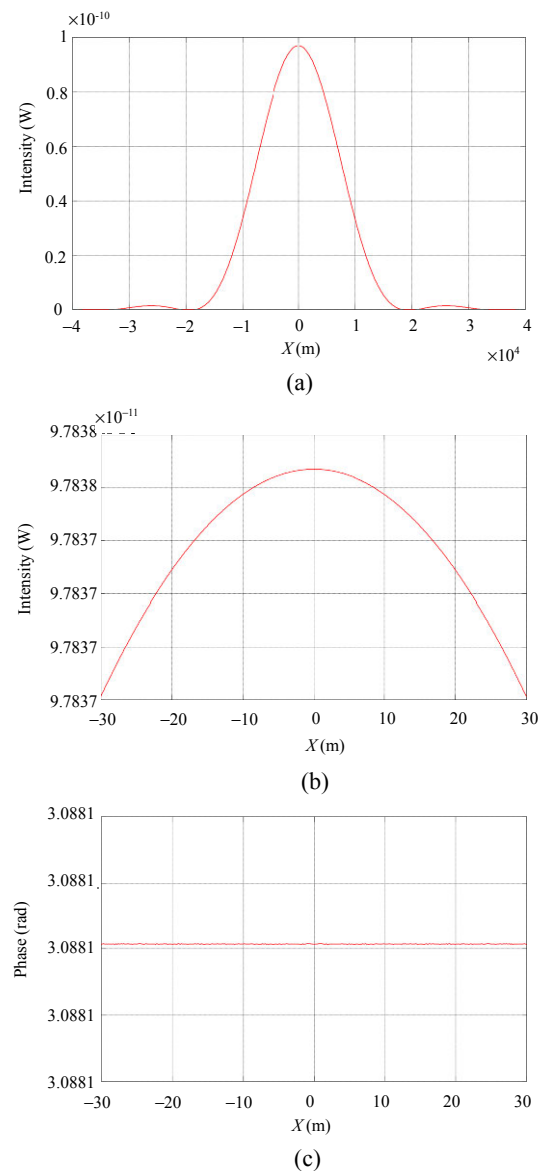

(a)

(b)

(c)

Fig. 1 Fair-field wavefronts: (a) the diffraction intensity distribution of the far field, (b) the intensity within a radius of 30 m that are vertical to the line of sight, and (c) the phase within a radius of 30 m that are vertical to the line of sight.

The aperture of the telescope is 200 mm, the wavelength is 1.064 μm, and the transmission distance is 3×10^9 m. The diffraction intensity distribution of the spot at 3×10^9 m can be calculated as shown in Fig. 1(a). The radius of the Airy disk corresponding to the zero-order fringe is close to 20 km. In the detection task of the Taiji Program, the jitter deviation of the exiting laser is required to be better than $8 \, \text{nrad} / \sqrt{\text{Hz}}$, and the distance of the far-end telescope from the visual axis caused by the jitter deviation is about ±24 m. Reduce the Fraunhofer diffraction integral area to ±30 m, and the results are shown in Fig. 7. The variance of intensity is 6.6341×10^{-32}, and the variance of phase is 9.2277×10^{-29}. Therefore, the beam received by the remote telescope can be regarded as a plane wavefront with uniform intensity and phase (the above is a simplified assumption, and interested readers could find more detailed discussions in [8–10], but these discussions are beyond the scope of this paper).

2.1.2 Interference between plane waves and Gaussian beams

A simplified schematic diagram of an interferometer is depicted in Fig. 2, which includes a flat-top beam, a Gaussian beam, and aquadrants photo diode (QPD). The flat-top beam could be regarded as a fraction of a plane wave. Here, we set a Gaussian beam as the reference beam that propagates along the z-axis and strikes the center of the detector. We also set a flat-top beam as the measurement beam that is tilted by an angle α around the y-axis, and to z_0 is the waist position. D and L are the diameter size and the gap size of the QPD, respectively.

In the physics of wave propagation, a plane wave is a wave whose wavefronts are infinite parallel planes and have equal field values in the surface along the direction of its propagation. The electric filed for an infinite plane wave can be given by

$$E(x, y, z) = A \cdot \exp\left[i(\mathbf{k} \cdot \mathbf{r} - \omega_1 t)\right]. \qquad (2)$$

Note that A is the amplitude and irrelevant for the pathlength signal, so set it to unity; ω_1 is the angular frequency; $\mathbf{k}$ is the wave vector and its direction is ordinary of which the plane wave is traveling, $|\mathbf{k}| = k = 2\pi / \lambda$, k is wavenumber; $\mathbf{r}$ is the position vector which defines a point in three-dimensional space. Figure 2 shows the direction cosine of $\mathbf{k}$ is $\cos(\alpha)$, $\cos(\beta)$, and $\cos(\gamma)$. In this situation, R can be regarded as dimension radius of the flat-top beam. A suitable expression of the flat-top beam is derived as (3), which is very simple to calculate the complex amplitude of the flat-top beam on the detector by replacing z as s in (3).

$$E(x, y, z)_{\text{flat}} = \begin{cases} \exp\left[-ik(x \sin\alpha + z \cos\alpha) + i\omega_1 t\right], & x^2 + y^2 \le R \\ 0, & \text{else.} \end{cases} \qquad (3)$$

Fundamental Gaussian beam is the most appropriate description for the output of most lasers. The amplitude of the electric field is also set to unity and Gouy phase is assumed as the static phase and ignored in the situation of Fig. 2, then the electric field can be written as

$$E_{\text{Gauss}}(x, y, z) = \exp\left(-i\omega_2 t - ik\frac{x^2 + y^2}{2q} - ik(z - z_0)\right) \qquad (4)$$

where the complex parameter is $q = (z - z_0) + iz_r$, the Rayleigh range is $z_r = \dfrac{\pi \omega_0^2}{\lambda}$, ω_0 is waist radius, z_0 is the z-axis value of the waist position, and ω_2 is the frequency.
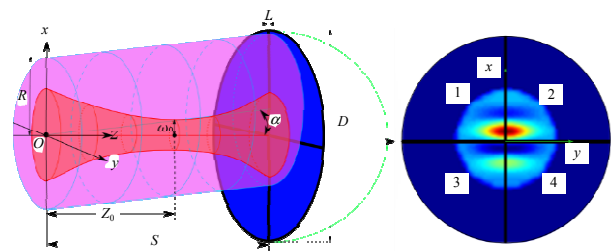

Fig. 2 Simplified schematic of an interferometer.

In the current theoretical analysis, the complex amplitude is normally used to calculate the phase information:

$$Int = \int_S E_{meas} E_{ref}^* dr^2 \qquad (5)$$

where E_{meas} and E_{ref}^* are respectively the field of the measurement beam and the reference beam, and Int is the integral result over the detection area.

The phase definition selected by LISA pathfinder is the LISA pathfinder (LPF) signal, which first sums the complex amplitudes of each quadrant of QPD and then uses the following argument:

$$\phi_{LPF} = \arg\left(\sum_{n=1}^{4} Int_n\right) \qquad (6)$$

where ϕ_{LPF} is the phase difference and n represents single quadrant. We focus here on the change in the optical path difference between the two beams. Because the path difference does not change over time, we can set $t = 0$ in the theoretical analysis. In addition, to simplify the calculations and obtain intuitive analytical solutions that clearly illustrate the parameter interdependency, we remove some of the terms that are unrelated to α from the calculation. First, we derive the analytical expressions for the complex amplitude of each quadrant on the detector. To research how the different factors are coupled into the measured path length, the final computation results will be visually decomposed into the sum of the different corresponding formulas in the simplification process. In Fig. 2, the flat-top beam is rotated along the y-axis, so quadrants 1 and 2 have the same field distribution, and quadrants 3 and 4 have the same field distribution:

$$Int_1 = Int_2 = \frac{1}{2}\int_{-R}^{R}\int_{\frac{L}{2}}^{R} E_{flat} E_{gauss}^* dxdy$$

$$\approx \frac{1}{2}\varepsilon\exp\left[ikz(1-\cos\alpha)+\frac{1}{2}ik(z_0-z)\right]\times$$

$$\sin^2(\alpha)\left[F\left(\frac{L}{2}\right)+F(R)\right] \qquad (7)$$

$$Int_3 = Int_4 = \frac{1}{2}\int_{-R}^{R}\int_{-R}^{-L/2} E_{flat} E_{gauss}^* dxdy$$

$$\approx \frac{1}{2}\varepsilon\exp\left[ikz(1-\cos\alpha)+\frac{1}{2}ik(z_0-z)\sin^2(\alpha)\right]\times$$

$$\left[F\left(-\frac{L}{2}\right)+F(-R)\right] \qquad (8)$$

$$F(r) = \mathrm{Erfi}\left[\frac{\left(\frac{1}{2}+\frac{i}{2}\right)\sqrt{k}\left[r-q\sin(\alpha)\right]}{\sqrt{q}}\right]. \qquad (9)$$

The longitudinal pathlength signal (LPS) resulted from LPF signal can then be derived as (ε represents the collection of terms that are unrelated to α and will be ignored in the following calculation)

$$LPS_{LPF} = \frac{\phi_{LPF}}{k} \approx -\frac{1}{2}s\alpha^2 + \frac{1}{2}(s-z_0)\alpha^2 +$$

$$\frac{\arg\left[2\left(F\left(\frac{L}{2}\right)+F(R)+F\left(\frac{-L}{2}\right)+F(-R)\right)\right]}{k}. \qquad (10)$$

We then set $L=0$ and give the idealized detector shape and integral area. Formulas are presented using Taylor expansions based on the premise of preserving the precision of the calculations to obtain more intuitive analytical expressions. LPS_{LPF} is then changed to

$$LPS_{LPF} \approx -\frac{1}{2}s\alpha^2 + \frac{1}{2}(s-z_0)\alpha^2 + O(\alpha^4). \qquad (11)$$

Next, we use numerical simulation tools to verify the correctness of above theoretical analysis results, the toolbox is named "TJOS" derived by "Taiji optical simulation", which is based on MATLAB and can imitate the procedures of the LTP phasemeter to compute interference signals. Then we use the numerical simulation tool "TJOS" to increase confidence in the correctness of above theoretical analysis. In the simulation, we set: $s = 500\,\mathrm{mm}$, $\omega_0 = 0.5\,\mathrm{mm}$, $R = 9\,\mathrm{mm}$, $D = 10\,\mathrm{mm}$, $L = 0$, and the waist position of Gaussian beam z_0 is respectively set to be $0\,\mathrm{mm}$ and $500\,\mathrm{mm}$ to observe the change of LPS_{LPF} with respect to the angle. The results are shown in Fig. 3,

which shows the simulation results are in good agreement with the analytical solution.

2.2 TTL introduced by the wavefront aberration of the telescope system

2.2.1 TTL caused by aberration

In the previous section, we analyzed the TTL coupling noise that was generated by the interference between an ideal flat-top beam and a Gaussian beam. However, there is no ideal telescope.

Design and alignment errors in the telescope can cause distortions in exit pupil wavefronts. Next, we will analyze the case of TTL coupling noise introduced by aberrations. The Zernike polynomials are used to fit the wavefront characteristics of the optical system. Since the high-order Zernike polynomials account for a small proportion, we usually consider the first eight terms of the Zernike polynomials, as shown in Table 1.
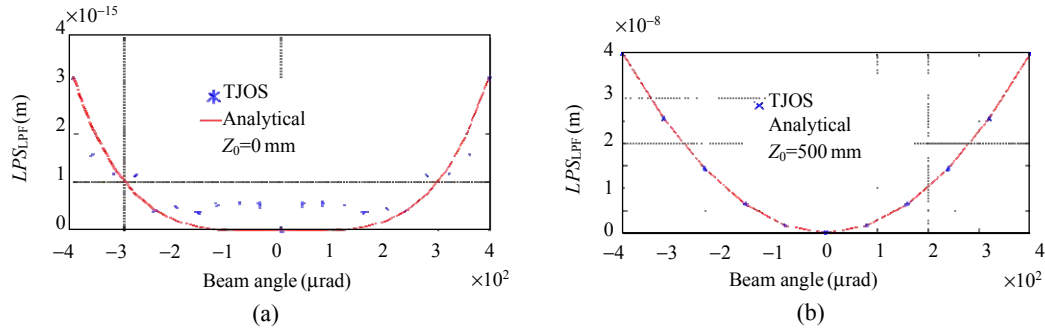

(a) (b)

Fig. 3 Change in LPS_{LPF} with respect to the angle α: (a) shows that when the waist position of Gaussian beam coincides with the rotation point of the flat-top beam, LPS_{LPF} is significantly below the picometer scale (the differences are numerical errors due to ray tracing algorithm) and (b) shows that when the waist position of the Gaussian beam concides with the position of detector, LPS_{LPF} is equal to the optical pathlength difference.

Table 1 Zernike polynomials.

Term	Polar coordinates	Cartesian coordinates	Corresponding aberration
z_1	$\rho\cos\theta$	x	Tilt x
z_2	$\rho\sin\theta$	y	Tilt y
z_3	$2\rho^2-1$	$-1+2(x^2+y^2)$	Defocus
z_4	$\rho^2\cos(2\theta)$	x^2-y^2	Astig x
z_5	$\rho^2\sin(2\theta)$	$2xy$	Astig y
z_6	$\rho(-2+3\rho^2)\cos\theta$	$-2x+3x(x^2+y^2)$	Coma x
z_7	$\rho(-2+3\rho^2)\sin\theta$	$-2y+3y(x^2+y^2)$	Coma y
z_8	$1-6\rho^2+6\rho^4$	$1-6(x^2+y^2)+6(x^2+y^2)^2$	Primary spherical

The complex amplitude representation of this measurement beam is as follows:

$$E\left(x,\,y,\,z\right)_{\mathrm{flat}}=$$
$$\begin{cases}\exp\left[-\mathrm{i}k\left(x\sin\alpha+z\cos\alpha\right)+\mathrm{i}\omega_1 t+\mathrm{i}2\pi\Delta W\right],\ & x^2+y^2\leq R \\ 0, & \text{else}\end{cases}$$
(13)

$$\Delta W=z_0+z_1 x+z_2 y+z_3\left[2\left(x^2+y^2\right)-1\right]+$$
$$z_4\left(x^2-y^2\right)+2z_5 xy+$$
$$z_6\left[3x\left(x^2+y^2\right)-2x\right]+$$
$$z_7[3y(x^2+y^2)-2y+$$
$$z_8[1-6(x^2+y^2)+6(x^2+y^2)^2].$$

where ΔW is the wavefront aberration caused by imperfect imaging. In the above formula, $z_0 \sim z_8$ are the first nine terms of the Zernike polynomials, z_0 is the piston aberration, which is not considered here. z_1 and z_2 are the tilt aberrations. Since the tilt factor is considered in the front part of the representation, the tilt aberration is not taken into account here. Therefore, we consider $z_3 \sim z_8$ in this paper. According to the real situation, we take each aberration into account separately in the simulation calculation and allow the aberration value to change

in $0 \sim \dfrac{\lambda}{10}$ and the step number to be $\dfrac{\lambda}{100}$. The extraction of the optical path signal is calculated by referring to the phase of the complex conjugate of the reference beam and the measurement beam as in the previous section. The simulation results of the optical path signal are shown in Fig. 4. The results show that any kinds of aberrations increase TTL noise, including the defocusing and spherical aberration that affects the optical path signal the most. The astigmatism and coma in the *y*-direction have less influence on it. The coma of *x*-direction creates the unbalanced situation in the change of TTL coupling noise with respect to the angle α.

2.2.2 TTL introduced by the wavefront aberration of the telescope system due to the in-orbit environment

In addition, the dimensional changes after the telescope is in the orbit (launch process overload, temperature gradient, stress release under microgravity, material outgassing, etc.) will exacerbate the distortion in the exit pupil wavefront. That means the wavefront entering the scientific interferometer has had distortions and will also bring in TTL coupling noise. When propagating in the off-axis telescope system, the flat-top wavefronts that are intercepted by the entrance pupil of the received telescope produce diffraction result in unevenwavefronts into the scientific interferometer.

According to the previously analyzed function and effect of the telescope and by considering the stringent requirements for stray light, the preliminary scheme of the optical system of the telescope adopts the off-axis four-mirror structure [in Fig. 5(a)], which is a 4-mirror optimized off-axis afocal Richey-Chrétian telescope with the exit pupil pushed outward to accommodate the interface to the optical bench. The primary mirror M1 is nearly parabolic, and the secondary mirror M2 is hyperbolic. M3 and M4 are spherical. The detailed optical system design parameters are shown in [8].
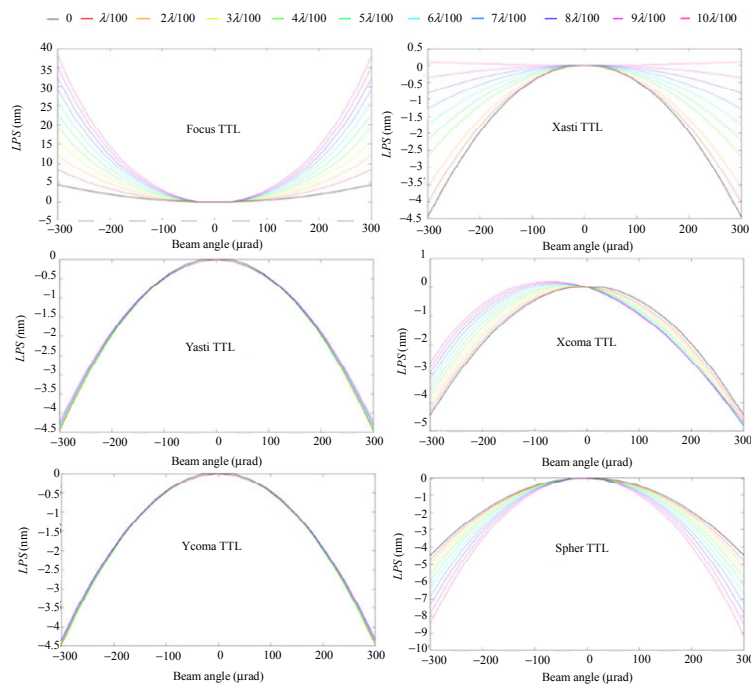

Fig. 4 LPS signals originated from 6 kinds of aberrations.

According to the analysis in Section 2, if the TTL noise needs be reduced, the wavefront quality at the exit pupil of the telescope should be as good as possible. Figure 5(b) shows the currently designed wavefront quality at the exit pupil, with the root mean square (RMS) of 0.013λ.
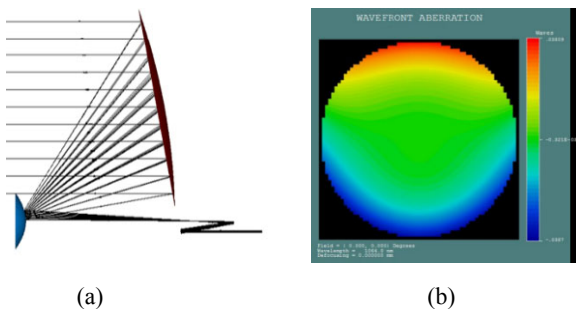
(a) (b)

Fig. 5 Optical design of the telescope and its wavefront in the exit pupil: (a) the 4-mirror telescope and (b) the wavefront in the exit pupil.

The opto-mechanical structure design of the telescope is shown in the left of Fig. 6. The mirror adopts zero-grade zerodure, and the structure is invar with the matching linear expansion coefficient. The right of Fig. 6 shows the structural deformation nephogram due to in-orbit temperature and gravity release. Figure 7 gives the surface shape nephogram of each mirror that was obtained by surface shape fitting, and the position change of each mirror is shown in Table 2. Each mirror shape and position changes were returned to the optical system for iteration. Here, the first nine terms of the Zernike polynomials were used to respectively fit an ideal wave surface and the wave surface after the opto-mechanical thermal analysis, and the sizes of the first nine Zernike coefficients were obtained, as shown in Table 3 (excluding the first term).
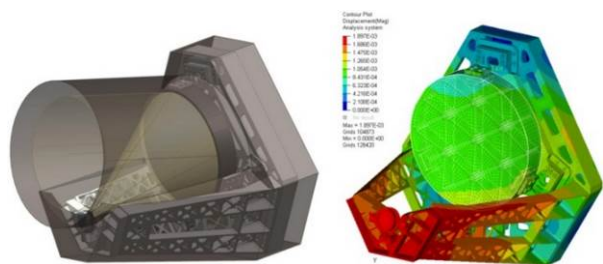

Fig. 6 Left is the opto-mechanical structure design of telescope prototype; the right is the structural deformation nephogram of the telescope prototype due to in-orbit temperature and gravity release.
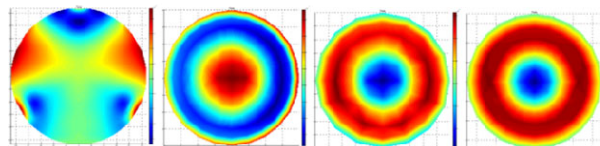

Fig. 7 Surface fitting nephogram of reflective mirrors, the order from left to right is M1, M2, M3, and M4.

Table 2 Change of surface shape and position of each mirror.

	M1	M2	M3	M4
PV (nm)	45.721	1.663	0.121	0.711
rms (nm)	8.927	0.503	0.032	0.183
ΔX (μm)	0.001	−0.369	−0.005	−0.024
ΔY (μm)	−0.403	0.977	0.497	−1.271
ΔZ (μm)	0.855	1.407	0.540	−0.988
$\Delta \theta x$ (″)	−0.363	−0.009	2.570	2.063
$\Delta \theta y$ (″)	0.104	−0.403	0.011	0.027

By analysis, in the in-orbit environment, the wavefront of the telescope system, as shown in Table 3, changed from $\lambda/60$ (rms) to $\lambda/50$ (rms), and each Zernike coefficient increased to different extents. Then, we used two wavefronts to interfere with Gaussian beams, respectively, and extract and compare the optical path noise with the data of the perfect flat-top beam. Here, W_p stands for the flat-top beam, W_{tel1} stands for the wavefront in an ideal optical system, and W_{tel2} stands for the wavefront after the opto-mechanical thermal integration analysis. The comparison results are shown in Fig. 8. It can be clearly seen from Fig. 8 that as the wavefront deteriorated, the optical path noise increased. According to the slope diagram of the optical path noise, if there is no other measure, the wavefront received by the telescope entered the scientific interferometer and interferes with the local Gaussian beam. Its rate of change in the optical path noise exceeded the TTL specification requirement, so effective measures must be taken to suppress TTL noise.

Table 3 Zernike coefficients of the wavefront of the telescope system before and after deformation.

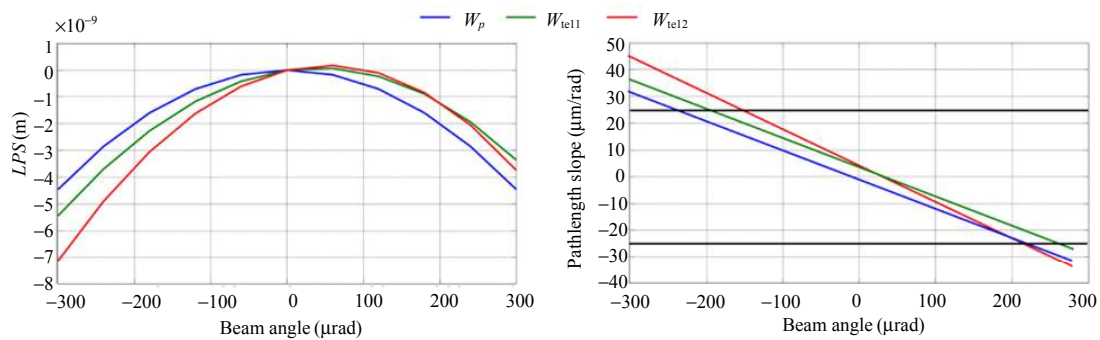| Zernike coefficient	z_1	z_2	z_3	z_4	z_5	z_6	z_7	z_8
Before deformation	0	−0.0279	−0.0035	−0.0065	0	0	−0.0135	−0.0013
After deformation	0.0002	−0.0404	−0.0052	0.0126	−0.0002	−0.0001	−0.0185	0.0027
Diff	0.0002	0.0125	−0.0017	0.0191	−0.0002	−0.0001	−0.005	0.004

Fig. 8 Optical path signals caused by the interference between the Gaussian beam and three different cases for the flat-top beam. Its rate of change in the optical path noise exceeds the TTL specification requirement of 25 μm / rad .

3. Imaging system for suppressing TTL coupling noise [8–11]

According to Fermat's principle, the optical paths of the rays between the conjugated object plane and the image plane in the imaging system are equal and irrelevant to the aperture angle. According to this feature, we can design a suitable imaging system to suppress the TTL coupling noise in the telescope system [9]. The specific method is to place an imaging system between the exit pupil of the telescope and the detector, so that the exit pupil of the telescope and the detector are in a conjugate relationship of objects and images. This can suppress the TTL coupling noise caused by the intersatellite mutual movement and the telescope system.

The following constraints must be considered when designing this imaging system:

(1) Due to the limitation of the installation space, the distance between the entrance and exit pupils and the distance between the detector and the final lens of the imaging system should be adjustable.

(2) The size of the exit pupil of the telescope is 5 mm, so the magnification of the imaging system needs be constrained to a certain range in order to ensure the energy of the beam on the detector and reduce the stray light caused by the edge of the detector.

(3) To reduce the extra optical path noise caused by the beam walk on the detector, the beam walk on the detector should be suppressed as much as

possible.

(4) Wavefronts of the telescope system have residual aberrations, so the exit pupil of the telescope is taken as the input of beams when optimizing the imaging system.

The final optimized imaging system parameters are shown in Table 4 (the exit pupil of the telescope is set to zero).

In this paper, consideration is only given to the contribution of the telescope system to TTL coupling noise. Suppose that the interferometer has no aberrations, so the system can be simplified to the one shown in Fig. 9. Only the telescope, local Gaussian beams, and the imaging system for suppressing TTL noise are contained.

Table 4 Parameters of imaging system.

	Unit	Lens 1	Lens 2	QPD
Position	mm	318.5085	426.6324	458.6078
The first surface curvature		14.897844		
The second surface curvature		13.946023	−12.334337	
Center thickness	mm	16.0232	15.7419	
Substrate radius	mm	5	5	0.5
Refractive index	1	1.44963	1.44963	

In the simplified simulation system shown in Fig. 9, the maximum field of view in the scientific mode of the telescope is ±7 μrad and is set to ±10 μrad in this paper. Since the magnification of the telescope is 40, the range of beam rotation at the entrance pupil of the imaging system for suppressing TTL noise is ±400 μrad. This simulation system is used to carry out three kinds of ray tracings (through

GBDC decomposition). In the first ray tracing, the assumption is that the wavefront of entrance pupil of the teleclope system is a perfect plane, and the result caused is represented by W'_p. The second is that the telescope system only has design tolerance and the wavefront quality is not affected by the environment, represented by W'_{tel1}. The third ray tracing of the telescope system, consideration is given to the telescope system after the influence of the in-orbit environment, represented by W'_{tel2}. The simulation results are shown in Fig. 10. The results show that due to the residual aberration of the wavefront at the exit pupil of the telescope, the optical path noise increases, and the suppression capability of the imaging system is the pathlength slope, which is 7μm/rad to the maximum. In view of the further deterioration of the wavefront quality at the telescope exit pupil after the in-orbit opto-mechanical thermal environment, the maximum pathlength slope after suppression by the imaging system is 12μm/rad. However, it is still within the required range of ±25 μm/rad.
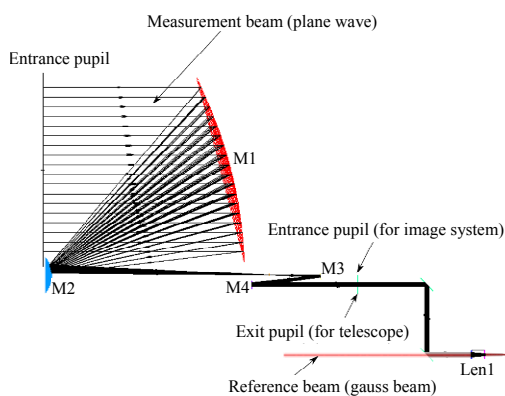

Fig. 9 Simplified schematic of telescope and optical bench. The entrance pupil of the telescope system concides with the exit pupil of image system.

The simulation results prove that this imaging system can meet the measurement requirements. In the future work, a system needs to be constructed to measure the contribution of the telescope system to the TTL coupling noise in the interferometry system, and the contribution of the processing error, aberration, and alignment tolerance of the interferometer components to the TTL coupling

noise in the interferometry system needs to be analyzed and studied. Decoupling the TTL coupling noise of the telescope system, the interferometer system provides the basis for the subsequent double-satellite mission, design, noise distribution, and engineering development in the Taiji Program [10].
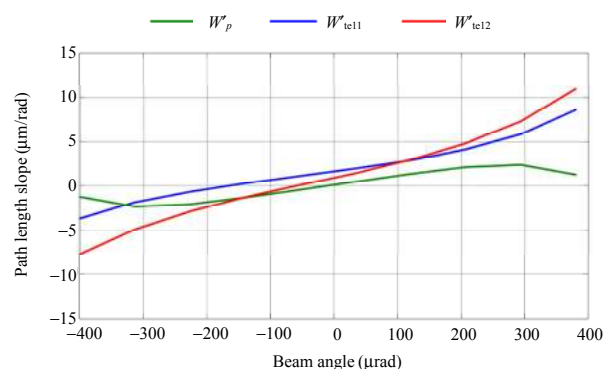

Fig. 10 Simulation results of path length slope caused by three different situations, respectively.

4. Conclusions

In this paper, we studied the TTL coupling noise that was introduced by the telescope system in the presence of the breathing angle in the million-kilometer long-baseline intersatellite laser interferometry system for the first time in the world. The flat-top beams intercepted by the telescope were affected by telescope magnification, residual aberrations, and diffraction. The wavefront distortions were caused by changes in the structural parameters of the telescope after entering the orbit (launch process overload, temperature gradient, stress release under microgravity, material outgassing, etc.).

We analyzed the mechanism of the TTL coupling noise that was introduced by the telescope. According to the simulation results of the scientific interferometry system, the TTL coupling noise that the telescope system introduced exceeded the technical requirements for gravitational wave detection in space and noise suppression measures must be taken. The designed imaging system for suppressing TTL coupling noise makes the TTL coupling noise suppression of the interferometry

system within the required range of the specifications, proving its effectiveness. In the follow-up work, the TTL coupling noise introduced by the scientific interferometer design, processing and alignment errors is firstly analyzed. Second, the TTL coupling noise measurement system is built, thus decoupling and measuring the TTL coupling noise of the telescope and the interferometer. This lays the foundation for the follow-up task design, key technology research, and engineering prototype development in the Taiji Program.

Acknowledgments

References

[1] S. L. Danilishin, E. Knyazev, N. V. Voronchev, F. Ya. Khalili, C. Gräf, S. Steinlechner, *et al*., "A new quantum speed-meter interferometer: measuring speed to search for intermediate mass black holes," *Light*: *Science & Application,* doi: 10.1038/s41377-018-0004-2.

[2] G. Wanner, "Complex optical systems in space: numerical modeling of the heterodyne interferometry of LISA pathfinder and LISA," Ph.D. dissertation, Max Planck Society, Germany, 2010.

[3] J. Livas and S. Sankar, "Optical telescope design study results," *Journal of Physics: Conference Series*, 2015, 610: 012029.

[4] S. Schuster, "Tilt-to-length coupling and diffraction aspects in satellite interferometry," Ph.D. dissertation Gottfried Wilhelm Leibniz Universität Hannover, Germany, 2017.

[5] S. Schuster, "Investigation of the coupling between beam tilt and longitudinal pathlength signal in laser interferometers," Master dissertation, Gottfried Wilhelm Leibniz Universität Hannover, Germany, 2013.

[6] S. Schuster, M. Tröbs, G. Wanner, and G. Heinzel, "Experimental demonstration of reduced tilt-to-length coupling by a two-lens imaging system," *Optics Express*, 2016, 24(10): 10466–10475.

[7] M. Chwalla1, K. Danzmann, G. F. Barranco, E. Fitzsimons, O. Gerberding, G. Heinzel, *et al*., "Design and construction of an optical test bed for LISA imaging systems and tilt-to-length coupling," *Classical and Quantum Gravity*, 2016, 33(24): 245015.

[8] Z. Wang, W. Sha, Z. Chen, Y. Kang, Z. Luo, L. Ming, *et al*., "Preliminary design and analysis of telescope for space gravitational wave detection," *Chinese Optics*, 2018, 11 (1): 131–151.

[9] M. Chwalla, K. Danzmann, G. F. Barranco, E. Fitzsimons, O. Gerberding, G. Heinzel, *et al*., "Design and construction of an optical test bed for LISA imaging systems and tilt-to-length coupling," *Classical and Quantum Gravity*, 2016, 33(24): 245015.

[10] Z. Luo, S. Bai, X. Bian, G. Chen, P. Dong, Y. Dong, *et al*., "Space laser interferometry gravitational wave detection," *Advances in Mechanics*, 2013, 43(4): 415–447.

[11] S. Schuster, M. Tröbs, G. Wanner, and G. Heinzel, "Experimental demonstration of reduced tilt-to-length coupling by a two-lens imaging system," *Optics Express*, 2016, 24(10): 10466–10475.